

SURROGATE MODEL TO PREDICT THE STAGNATION POINT WALL HEAT FLUX DURING COMPOSITE MATERIAL DEGRADATION

Maxime Lalande, Nicolas Dellinger⁽¹⁾, Nathalie Bartoli⁽²⁾, and Julien Annaloro⁽³⁾

⁽¹⁾DMPE, ONERA, Université de Toulouse, 31000, Toulouse, France

⁽²⁾DTIS, ONERA, Université de Toulouse, 31000, Toulouse, France

⁽²⁾Fédération ENAC ISAE-SUPAERO ONERA, Université de Toulouse, 31000, Toulouse, France

⁽³⁾Centre National d'Études Spatiales, 31000, Toulouse, France

ABSTRACT

A surrogate model is developed to predict the influence of pyrolysis gas blowing on wall heat flux in the continuous hypersonic regime, for atmospheric re-entry of COPV space debris from Low Earth Orbit. Five input variables representative of the flight conditions (freestream density and speed), wall conditions (temperature, blowing rate) and geometry (nose radius) for a given pyrolysis gas composition are considered. The training database is made up of roughly 1000 CFD simulations, with two modeling approaches referred to as “low-fidelity” (CFD-LF) and “high-fidelity” (CFD-HF) respectively. The surrogate model is developed using Multi-Fidelity Kriging methods, which take advantage of CFD-LF and CFD-HF simulations simultaneously. The model is validated on a distinct dataset with low prediction errors and is implemented in an atmospheric re-entry code. Full atmospheric re-entry trajectories of COPV are simulated with this model, and reveal an increase of about 30 % in the integrated flux at the stagnation point over the entire continuous regime. This demonstrates the major influence of pyrolysis gas blowing along a complete trajectory, which is usually neglected in atmospheric re-entry codes.

Keywords: Aerothermodynamics, Material degradation, Atmospheric re-entry, Surrogate Model, Kriging.

1. INTRODUCTION

While some part of space debris disintegrates during atmospheric re-entry, some may survive and pose a ground risk. According to ESA, a third of the recovered debris are Composite Overwrapped Pressure Vessels (COPV) [1], *i.e.* tanks made of an inner metal liner and an external Carbon Fiber Reinforced Polymer (CFRP) layer. When submitted to the significant aerothermal heating as the one encountered during the re-entry, this kind of composite materials degrades and ablation gases are released into the boundary layer. The blowing of ablation species modifies the chemical composition of the flow and affects

the wall heat flux. Thus, there is a strong physical coupling between the flow and the thermochemical response of the material.

All these phenomena can be faithfully modeled using high-fidelity codes, such as CFD and material response codes [2, 3, 16, 25]. Recently, Lalande et al. [17, 18] investigated the influence of pyrolysis gas blowing on convective-diffusive wall heat flux, for atmospheric re-entry of COPV from LEO. For that, CFD simulations in chemical non-equilibrium with 28 species and 131 reactions have been carried to investigate the influence of the blowing rate and the reactions between the degassed species and the air. It is shown that the wall heat flux can either be reduced by the convective blocking effect of the blowing, or increased up to a factor 2 because of the strong exothermal chemical reactions occurring between the ablation byproducts and the air species in Earth atmosphere. Even though CFD codes enable to model these phenomena, such tools are too costly for complete trajectory calculations. Correlations employed in atmospheric re-entry codes allow for rapid modeling of vehicle aerothermodynamics; however, they do not account for complex gas-surface interactions as the ones described previously.

This paper presents the development and exploitation of a surrogate model to predict the influence of pyrolysis gas blowing on wall heat flux modification, in the continuous hypersonic regime, for COPV space debris re-entering the atmosphere from LEO. First, the methodology followed for the training and validation of the model is described in Section 2. In Section 3, the model is implemented in the atmospheric re-entry code ARES, and space debris re-entry simulations are performed in order to assess the influence of pyrolysis gas blowing along a complete trajectory.

2. DEVELOPMENT OF A SURROGATE MODEL USING MULTI-FIDELITY KRIGING

In this section, a surrogate model is developed using supervised machine learning methods to predict the influ-

ence of pyrolysis gas blowing on stagnation point wall heat flux. Firstly, the choice of the Multi-Fidelity Kriging (MFK) learning method is justified in accordance with the problem to be modeled. A design of experiments is defined so as to generate a numerical database, made of CFD simulations. The model is trained on the learning dataset, and prediction errors are evaluated on an independent validation dataset.

2.1. Selection of the supervised machine learning method

A wide variety of supervised machine learning methods are used in the literature to develop surrogate models predicting the convective-diffusive heat flux, based on training databases made up of CFD simulations [11, 31, 35]. The choice of the type of model to be trained is a crucial first choice, and must be made according to various criteria; such as the nature (continuous, categorical) of the inputs/outputs, the dimension of the problem, and the size of the learning base that can be generated.

In this work, we aim to predict the stagnation point wall heat flux ϕ_{stag} taking into account the influence of pyrolysis gas blowing. Numerous correlations already exist in the literature to calculate the stagnation point heat flux without blowing $\phi_{NB,stag}$ [7, 10, 13, 29, 33, 36, 37]. We have therefore chosen to develop a surrogate model predicting the modification of the stagnation wall heat flux due to the blowing of pyrolysis gases $(\phi/\phi_{NB})_{stag}$. Thus, the evaluation of ϕ_{stag} is based on the use of a model from the literature for $\phi_{NB,stag}$ and the new surrogate model for $(\phi/\phi_{NB})_{stag}$, as schematized in Figure 1.

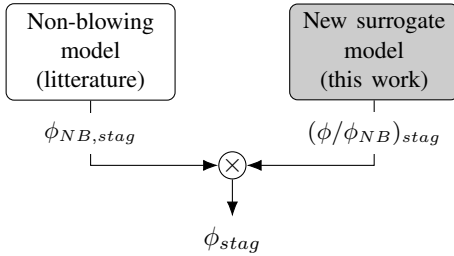


Figure 1: Strategy to calculate the stagnation point wall heat flux with blowing effects ϕ_{stag} , defined as the product of $\phi_{NB,stag}$ and $(\phi/\phi_{NB})_{stag}$. The gray block represents our contribution for modeling $(\phi/\phi_{NB})_{stag}$.

The objective is therefore to develop a surrogate model providing an estimation of $(\phi/\phi_{NB})_{stag} = f(\mathbf{x})$, with \mathbf{x} the inputs to be identified. A physical analysis of the influence of pyrolysis gas blowing was carried out in previous work using CFD simulations, and showed that $(\phi/\phi_{NB})_{stag}$ depends on several physical and geometric parameters [18]:

- The object’s geometry around the stagnation point affects the shock standoff distance and therefore the thermochemical state of the flow in the shock layer

near the stagnation point. This can be represented by the curvature radius evaluated at the stagnation point $R_{c,stag}$, also known as the nose radius R_N .

- Flight conditions also influence the thermochemical state of the shock layer. This can be represented by the velocity of the object V_∞ and the density of the freestream air ρ_∞ , which characterises the altitude z .
- Wall conditions, such as wall temperature T_w and pyrolysis gas mass rate \dot{m} .
- The composition of pyrolysis gases influences the chemical reactions taking place in the boundary layer between air and degassed species, and the chemical composition close to the wall.

In a first approach, the influence of the chemical composition of pyrolysis gases is neglected, *i.e.* the model is developed under the assumption of a fixed outgassing composition, see Section 2.4. Although the composition has an important influence on the evaluation of $(\phi/\phi_{NB})_{stag}$, its characterization significantly increases the dimension of the problem. Indeed, for a mixture of a maximum of N_s species, this would require adding N_s inputs to the model. As a result, only the influence of geometry at the stagnation point, flight conditions and wall conditions are considered. These parameters are represented by five scalar inputs $\mathbf{x} = (R_N, V_\infty, -\ln(\rho_\infty), T_w, \dot{m})$.

Finally, the preliminary analysis carried out showed that in the presence of pyrolysis gas blowing, the accuracy of the diffusion coefficients used for CFD simulations has a major influence on the wall heat flux evaluation [18], but their faithful modeling can have a significant CPU cost. Two types of CFD simulations have been conducted: the species diffusivity was either directly computed from a Schmidt number per species (lower fidelity approach), or obtained from the full resolution of the diffusion linear system thanks to collision integral calculations (higher fidelity approach). In the following, the two modeling approaches are referred to as “low-fidelity” CFD simulations (CFD-LF) and “high-fidelity” CFD simulations (CFD-HF) respectively. A discrepancy up to 15 % is observed between the two methods, with a CPU-cost approximately twice as high for CFD-HF as for CFD-LF simulations.

Thus, the supervised learning method chosen is Multi-Fidelity Kriging (MFK), also known as Multi-Fidelity Gaussian Process [20]. This method is an interpolation technique using data of varying accuracies during the training process, in order to improve predictions and reduce the budget of the database generation. It requires less training points than neural-network approaches. Moreover, a Gaussian process is a stochastic process [30]. It provides a probabilistic prediction, *i.e.* a mean prediction \hat{y} and the associated variance prediction σ^2 . The uncertainty evaluation is valuable in the framework of space debris re-entry risk analysis. Moreover, it enables to perform adaptative model enrichment in poorly predicted area of the design space. The

multi-fidelity approach enables to take advantage of both CFD-LF and CFD-HF simulations to build a more accurate predictive model. In this work, we used the Surrogate Modeling Toolbox (SMT 2.0) [34] to sample the dataset and train the surrogate model. The MFK modeling method used is based on the auto-regressive formulation of Le Gratiet [20], which requires nested training points.

2.2. Multi-Fidelity Kriging

Let f be the target function we wish to estimate:

$$f: \mathcal{D} \subset \mathbb{R}^5 \rightarrow \mathbb{R}$$

$$\mathbf{x} \mapsto f(\mathbf{x})$$

with \mathbf{x} a vector of inputs from the design space \mathcal{D} . Thus, $f(\mathbf{x})$ is estimated by a realization of a Gaussian Process (GP) Y , with mean m and covariance function k [30]:

$$Y \sim \mathcal{GP}(m, k) \quad (1)$$

After optimization of the hyperparameters of the GP by best fit of the model to the target function, the model can be exploited to make new predictions, consisting of a mean prediction $\hat{y}(\mathbf{x})$ and associated variance prediction $\sigma^2(\mathbf{x})$. This approach can be extended to the multi-fidelity framework, and is detailed for two fidelities in the following. Let f^{LF} and f^{HF} be two target functions simulating the same physical phenomena, with f^{HF} more accurate but also more costly than f^{LF} . Thus, more observations of f^{LF} can be done, but with lower accuracy. These two functions are both estimated by a realization of a Gaussian Process Y^{LF} and Y^{HF} . The auto-regressive model of Le Gratiet [20] is then defined by:

$$Y^{HF}(\mathbf{x}) = \rho(\mathbf{x})Y^{LF} + \gamma(\mathbf{x}) \quad (2)$$

where $\rho(\mathbf{x})$ is a scaling factor between Y^{LF} and Y^{HF} , and $\gamma(\mathbf{x})$ is the discrepancy function to capture the difference between the two models. More details can be found in [20].

2.3. Design of Experiments

A design of experiments has been established to generate the training and validation database of the model. First, the validity limits of the 5 inputs are defined in order to delimit the design space, see Table 1. These intervals correspond to conditions that may be encountered during the hypersonic continuous regime phase of atmospheric re-entry of a wide range of COPV debris from LEO. They have been identified using the ARES atmospheric re-entry code [28]. These trajectories simulations have been carried out considering an injection velocity

$V_\infty = 7.7 \text{ km} \cdot \text{s}^{-1}$ at initial break-up altitude $z = 78 \text{ km}$, for objects of various shapes and dimensions. The input interval $-\ln \rho_\infty$ corresponds to an altitude $z = 30 - 78 \text{ km}$. [18].

Table 1: Design space for the surrogate model development.

Input	Range
R_N	0.1 – 5.5 m
V_∞	1.5 – 7.7 km · s ⁻¹
$-\ln \rho_\infty$	3.99 – 10.59
T_w	500 – 2500 K
\dot{m}	0 – 20 × 10 ⁻³ kg · m ⁻² · s ⁻¹

The database is sampled using the Latin Hypercube Sampling (LHS) method, which selects points pseudo-randomly and uniformly distributed in the design space. To ensure that CFD-LF and CFD-HF points are nested, two nested LHS are generated:

- LHS of 800 points for CFD-LF simulations.
- LHS of 200 points for CFD-HF simulations.

In addition, a validation database separate from the training database is generated to evaluate the model's prediction error. This is made up of 150 CFD-HF points, defined using the LHS method.

2.4. Numerical database

The CFD code used in this work is the unstructured cell-centered finite volume Navier-Stokes solver CHARME, which is part of the multi-physics platform CEDRE [32]. For the considered conditions, the flow is assumed to be non-ionised and in thermal equilibrium. Chemical non-equilibrium between dissociated air and ablation species is accounted for using a kinetic model of 131 reactions and 28 neutral species derived from the work of Martin et al. [26]. Individual species viscosity and conductivity are computed from Blotter's curve fits and Prandtl number [19]. Mixture properties are then calculated using Wilke's mixing rule [39]. For CFD-LF simulations the species diffusivity is directly computed from a Schmidt number per species. For CFD-HF simulations, the full diffusion linear system is solved thanks to collision integral calculation, using the EGLIB library [8, 9]. The inviscid (Euler) fluxes are computed using an AUSM+ [23] upwind scheme with second order multislope MUSCL reconstruction [21] and Van Leer limiter. Second order central difference [22] is employed for the viscous (Navier-Stokes) fluxes. For time marching, an implicit Euler scheme is used.

On the solid wall, a blowing boundary condition with zero pressure gradient and isothermal surface is considered. The mass blowing rate $\dot{m} = \rho_w v_w$, wall temperature T_w and blowing composition are prescribed. The

temperature of blown species is supposed to be equal to wall temperature $T_{blow} = T_w$. In case of zero mass blowing rate $\dot{m} = 0 \text{ kg} \cdot \text{m}^{-2} \cdot \text{s}^{-1}$ (non-blowing case), the wall is considered to be non-catalytic. The chemical composition of pyrolysis gas is taken from the work of Torres-Herrador et al. [38], who experimentally characterised the decomposition gases of an epoxy resin used in CFRP for COPV conception, under different conditions, for a temperature range $T = 573 - 1073 \text{ K}$. We have chosen the mixture characterised during the Py600-R800 test, in which the material was degraded at a pyrolysis temperature of 600°C (873 K) and the decomposition gases analysed in a second reactor at 800°C (1073 K). We believe that these conditions best represent the degradation of a CFRP during atmospheric re-entry, since the gases are first produced inside the material and then heat up as they are transported to the fluid-solid interface where they are finally ejected into the boundary layer. In their work, 70 species were identified, but we have only retained the major species involved in Martin's reaction mechanism. The composition considered is a mixture of (H_2 , H_2O , CO , CO_2 , CH_4) with mass fractions of (0.017, 0.283, 0.358, 0.093, 0.249) respectively.

The numerical database is only made of CFD simulations of 2D axisymmetric sphere of radius R_N . For each entry $\mathbf{x} = (R_N, V_\infty, -\ln(\rho_\infty), T_w, \dot{m})$ of the database, multiple simulations can be carried out:

1. Non-blowing reference case ($\dot{m} = 0 \text{ kg} \cdot \text{m}^{-2} \cdot \text{s}^{-1}$), to evaluate $\phi_{NB,stag}$.
2. CFD-LF with blowing, to evaluate ϕ_{stag}^{LF} , and thus $(\phi/\phi_{NB})_{stag}^{LF}$.
3. CFD-HF with blowing, to evaluate $(\phi/\phi_{NB})_{stag}^{HF}$.

The difference in wall heat flux between CFD-LF and CFD-HF is very small for non-blowing cases [18], so these simulations are carried out using CFD-LF modeling.

2.5. CFD simulations post-processing

The 800 CFD-LF and 200 CFD-HF points of the training dataset, as well as the 150 CFD-HF of the validation dataset, have been simulated following the methodology aforementioned. Figures 2 and 3 represent two examples of wall heat flux distribution along the wall. For a sphere, maximum heat transfer is expected to be reached at the stagnation point ($y/R = 0$), with a zero tangent. This is indeed the case for the first example shown in Figure 2. However, this is not true for the example shown in Figure 3. This deviation at the stagnation point is due to the inaccuracy of the numerical schemes to reconstruct the Euler fluxes through the shock layer close to the stagnation line. Numerous works in the literature report similar issues to accurately predict stagnation point wall heat flux for blunt objects in the hypersonic regime

[4, 12, 14, 15]. Further investigation has shown no improvement with mesh quality and/or refinement. Therefore, to keep the database generation as easy as possible, a smoothing is applied to the wall heat flux distribution for cases with consistent heat flux distribution along the wall, as represented by dashed lines in Figures 2 and 3, other cases being excluded from the database. For valid cases, the heat flux is extracted with the constraint of a zero tangent at the stagnation point, to calculate $(\phi/\phi_{NB})_{stag}$:

$$\left. \frac{\partial \phi}{\partial y} \right|_{y/R=0} = 0 \quad (3)$$

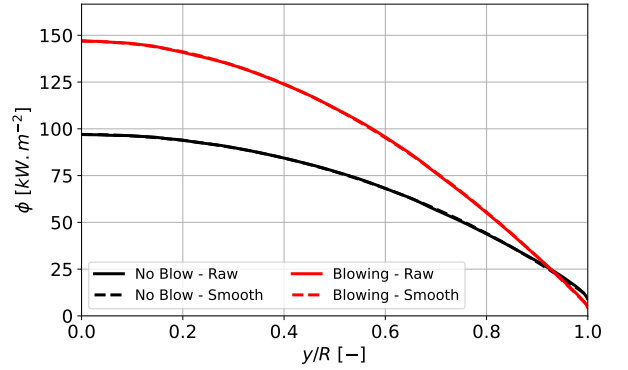


Figure 2: Wall heat flux distribution with (red lines) and without (black lines) blowing. Solid lines: raw results extracted from CFD simulations. Dashed lines: smoothed distribution with zero tangent at stagnation point. Case: $R_N = 1.2 \text{ m}$, $z = 76.2 \text{ km}$, $V_\infty = 5993.3 \text{ m} \cdot \text{s}^{-1}$, $T_w = 1153 \text{ K}$, $\dot{m} = 3.3 \times 10^{-3} \text{ kg} \cdot \text{m}^{-2} \cdot \text{s}^{-1}$.

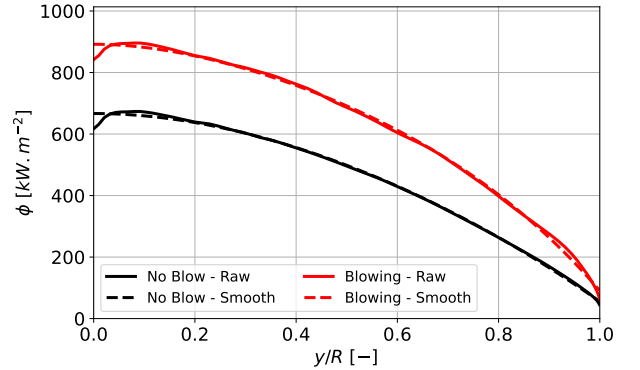


Figure 3: Wall heat flux distribution with (red lines) and without (black lines) blowing. Solid lines: raw results extracted from CFD simulations. Dashed lines: smoothed distribution with zero tangent at stagnation point. Case: $R_N = 0.83 \text{ m}$, $z = 30.9 \text{ km}$, $V_\infty = 3532.2 \text{ m} \cdot \text{s}^{-1}$, $T_w = 1974 \text{ K}$, $\dot{m} = 17.8 \times 10^{-3} \text{ kg} \cdot \text{m}^{-2} \cdot \text{s}^{-1}$.

In the end, of the 800 CFD-LF and 200 CFD-HF points in the learning database, only 708 CFD-LF and 180 CFD-HF points were used. Of the 150 CFD-HF points in the validation database, only 135 were used.

2.6. Training and prediction errors evaluation

The surrogate model is trained on 708 CFD-LF and 180 CFD-HF points. Several correlation functions are available in SMT [34], and the Matérn 5/2 kernel is used since it gives the most accurate prediction. Figure 4 shows the model's prediction on the 180 CFD-HF data used during training, to ensure that the model is correctly interpolating on its high-fidelity training data. This is necessary to guarantee the quality of the training process. Each red point corresponds to a point \mathbf{x} in the database, with y_{true} the true value of the associated output (result of the CFD calculation, used to train the model), and \hat{y} the model's prediction for this point. Thus, a point on the blue diagonal ensures that the model is interpolating. A very small dispersion is indeed observed for the 180 CFD-HF points of the training dataset, which is characterised by a low relative mean-square error (RMSE) of 9.3×10^{-7} , defined as:

$$\text{RMSE} = \frac{\|\hat{y} - y_{true}\|_2}{\|y_{true}\|_2} \quad (4)$$

with $\|\cdot\|_2$ the L2-norm calculated over the 180 CFD-HF points of the training dataset. Moreover, the 99% confidence interval ($\pm 3\sigma$) is very narrow, indicating that the model is interpolating on this training data.

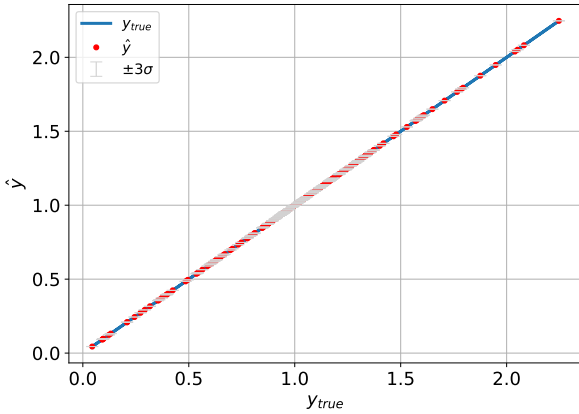


Figure 4: Correlation between the surrogate model prediction \hat{y} and corresponding true value y_{true} , evaluated on the 180 CFD-HF points of the training dataset. Grey error bars correspond to 99% confidence interval.

The model's prediction error is evaluated using the validation database, made up of 135 CFD-HF points. Model prediction on this dataset is shown in Figure 5. Overall, the points are relatively close to the diagonal, and only a few are significantly scattered. The prediction error is evaluated using the RMSE, estimated to be 19.21% on the validation dataset.

The points of the validation base for which the prediction error is the greatest, i.e. the points furthest from the diagonal on Figure 5, have been identified. These are cases for which the heat transfer at the stagnation point without blowing $\phi_{NB,stag}$ is relatively low, which depends on

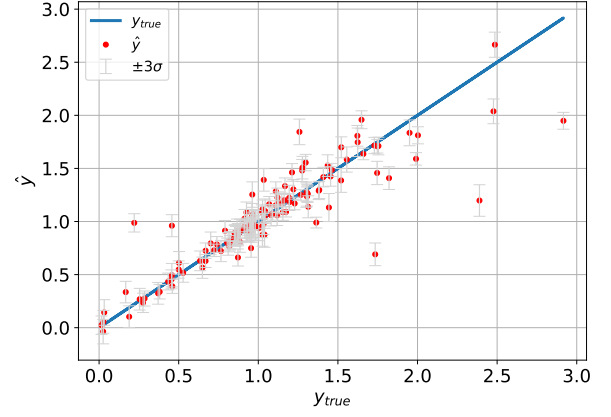


Figure 5: Correlation between the surrogate model prediction \hat{y} and corresponding true value y_{true} , evaluated on the 135 CFD-HF points of the validation dataset. Grey error bars correspond to 99% confidence interval.

several model inputs, since $\phi_{NB,stag} \propto \sqrt{\rho_\infty/R_N} V_\infty^3$ [6, 36]. To verify this, the RMSE of the model is evaluated on a reduced part of the dataset, eliminating points for which $\phi_{NB,stag}$ is below a given threshold. Figure 6 shows the evolution of the model's RMSE as a function of this threshold value. It can be seen that the prediction error falls rapidly for $\phi_{NB,stag} \geq 30 \text{ kW} \cdot \text{m}^{-2}$, then remains constant around 10% for $\phi_{NB,stag} \geq 50 \text{ kW} \cdot \text{m}^{-2}$.

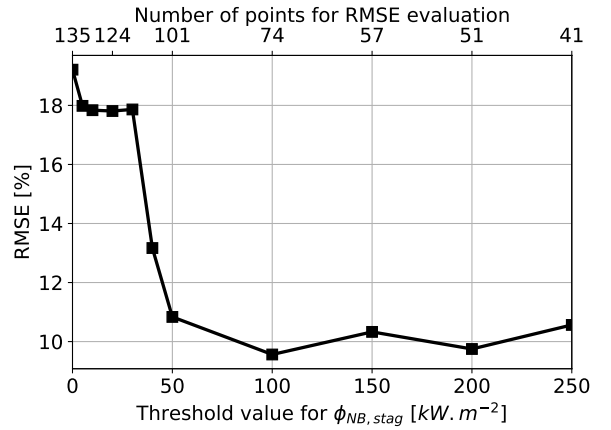


Figure 6: Surrogate model RMSE evaluated on the reduced validation dataset, with respect to the threshold value for $\phi_{NB,stag}$.

As a reminder, the purpose of the surrogate model is to evaluate the wall heat flux during the thermochemical degradation of CFRP, which is directly driven by heat transfer. It is therefore of limited relevance if the model is accurate for low heat fluxes such as $\phi_{NB,stag} \leq 50 \text{ kW} \cdot \text{m}^{-2}$, since there is little or no degradation. Figure 7 shows the model's prediction on the validation dataset, reduced to 101 CFD-HF points verifying $\phi_{NB,stag} \geq 50 \text{ kW} \cdot \text{m}^{-2}$. Prediction error is then

10.84%, which is comparable to that of surrogate models from the literature for the evaluation of the stagnation point heat flux without blowing for a non-catalytic wall [29].

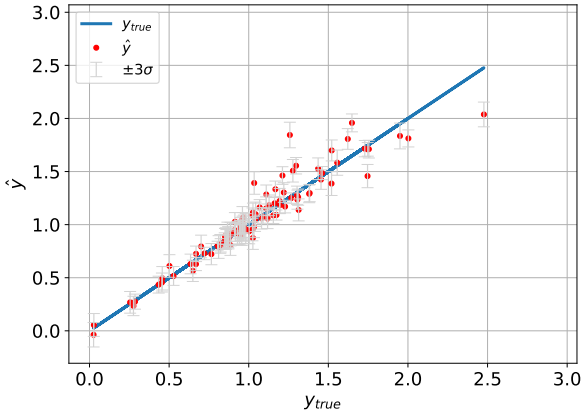


Figure 7: Correlation between the surrogate model prediction \hat{y} and corresponding true value y_{true} , evaluated on the 101 CFD-HF points of the reduced validation dataset, with $\phi_{NB,stag} \geq 50 \text{ kW} \cdot \text{m}^{-2}$. Grey error bars correspond to 99% confidence interval.

3. EVALUATION OF PYROLYSIS GAS BLOWING EFFECTS ALONG A COMPLETE RE-ENTRY TRAJECTORY

Now that a surrogate model has been developed to predict the evolution of $(\phi/\phi_{NB})_{stag}$, it is implemented in an atmospheric re-entry code. Complete atmospheric re-entry simulations are now carried out to analyse the influence of pyrolysis gas blowing on the entire trajectory.

3.1. Surrogate model implementation in an atmospheric re-entry software

Atmospheric entry simulations are performed using the code ARES [28], in which 4 independent solvers are coupled:

- **AtMoS** (Atmosphere Model Software) is based on various models of the Earth's atmosphere (US-62, US-76, US-76+Barlier, Jacchia 77, NRLMSIS-00) and the Martian atmosphere (MCD) to provide atmospheric conditions (pressure, temperature, density, etc.) as a function of position in space (altitude, longitude, latitude) and other parameters such as date, space disturbances, etc.
- **FAST** (Fast Aerothermodynamic Solver for Trans-atmospheric vehicle) contains various aerothermodynamic and aerodynamic models for calculating the wall convective-diffusive heat flux distribution,

as well as pressure and friction coefficients, for all flow regimes (hypersonic rarefied to continuous, and hypersonic to subsonic).

- **MUSIC** (Multi Simulators in Combination) is a 3 or 6 degree-of-freedom flight mechanics code. It uses the aerodynamic coefficients provided by FAST to calculate the trajectory of one or more synchronous or non-synchronous, guided, controlled or uncontrolled spacecraft, for orbital flight, rendezvous operation or atmospheric re-entry.
- **MoDeTheC** (in french: *Modèle de Dégradation Thermique des Composites*) solves the heat and mass transfers as well as thermal degradation within the material, using a multi-component approach [5].

The surrogate model developed in this work has been implemented in FAST for the continuous hypersonic regime. This means the model is only called for a Knudsen number $\text{Kn} \leq 10^{-3}$ and a velocity $V_\infty \geq 1.5 \text{ km} \cdot \text{s}^{-1}$. Otherwise, the heat flux ratio is set to $(\phi/\phi_{NB})_{stag} = 1$.

The evaluation of the stagnation point wall heat flux $\phi_{NB,stag}$ is done using correlations from the literature, see Figure 1. Since our surrogate model has been trained on CFD simulations assuming a non-catalytic wall, one needs to use a correlation for $\phi_{NB,stag}$ valid for non-catalytic wall. The stagnation wall heat flux is computed using the Fay-Riddell correlation [10] with the correction of Préveraud et al. [29] for non-catalytic wall. According to authors, the prediction error on $\phi_{NB,stag}$ is evaluated to 9.20%. However, there is no model available in FAST to calculate the wall heat flux distribution along the surface for non-catalytic walls. As a result, the analysis is limited to the stagnation point in the following. The same distribution model is used with and without activation of the new surrogate model for $(\phi/\phi_{NB})_{stag}$, to isolate the effects of pyrolysis gas blowing.

3.2. Complete atmospheric re-entry simulations of COPV taking into account the influence of pyrolysis gas blowing

The influence of pyrolysis gas blowing along a complete trajectory is evaluated by simulating the atmospheric re-entry of various representative COPV objects. These include hollow sphere, spherical-cylinder and a fuel tank geometry from the JAXA [24], see Figure 8. These objects are composed of an external Carbon Fiber Reinforced Polymer (CFRP) composite layer of thickness $e_{CFRP} = 10 \text{ mm}$ and an inner metal liner in TiAl6V4 of $e_{Li} = 1 \text{ mm}$. The CFRP is the aerospace composite M55J/M18 [27]. The composite is described by 4 components (M18 matrix, M55J fibers, char, pyrolysis gas) whose relative composition evolves as a function of the advancement state of a pyrolysis reaction [5]. Simulations are initialised with atmospheric conditions at altitude $z = 78 \text{ km}$, an injection velocity $V_\infty = 7.8 \text{ km} \cdot \text{s}^{-1}$,

and an initial slope angle $\gamma = -0.1^\circ$. Depending on the case, their might be an angle of attack α for the objects (apart from the sphere), see Figure 9. The dimensions, initial mass m_{ini} and angle of attack α of each considered case are given in Table 2.

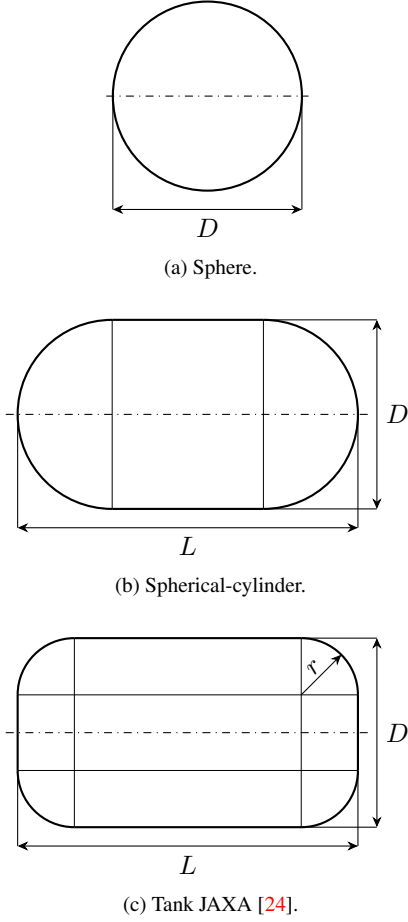


Figure 8: Sketch of the COPV geometries considered.

The results for case Sphere #4 ($D = 1.2$ m) are shown in Figure 10. Solid red lines correspond to complete atmospheric re-entry trajectories simulated using ARES, with activation of the surrogate model developed in this work. As MFK provides a stochastic prediction, the 99% confidence interval is represented by the grey area. CFD simulations are performed with and without pyrolysis gas blowing on 13 extracted flight conditions (black symbols) to compare with ARES' prediction, see Table 3. Trajectories computed without activation of the model are represented by the solid blue lines for reference. The evolution of wall heat flux at stagnation point is represented in Figure 10a. A significant increase in heat transfer can be observed over the entire phase of the continuous hypersonic regime of re-entry. At altitude $z = 61$ km, the heat flux peak increases from $334 \text{ kW} \cdot \text{m}^{-2}$ to $435 \text{ kW} \cdot \text{m}^{-2}$. This leads to a noticeable increase in wall temperature of around 100 K and a slight increase in pyrolysis gas blowing, see Figures 10c and 10d. The integral of the wall heat flux at stagnation point during the continuous regime is computed for all considered objects and reported in Ta-

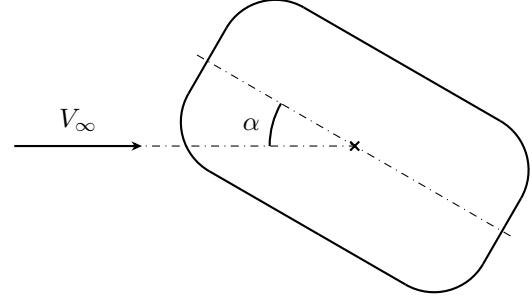


Figure 9: Sketch of a space debris with an incidence α .

ble 4. This metric quantifies the energy received by the object at its stagnation point during re-entry, and is increased by 33.7% for Sphere #4. This demonstrates the major influence of pyrolysis gas blowing along the trajectory. Wall degradation processes such as oxidation are not taken into account in our ARES simulations, but it would be interesting to see to what extent the increase in heat transfer and wall temperature is associated with an amplification of ablation phenomena.

The ARES re-entry simulation without activation of the surrogate model (blue curve) should fit the non-blowing CFD simulations (black triangles), and so the ARES simulations with the model (red curve) with the blowing CFD simulations (black squares). There is a noticeable discrepancy between the ARES and CFD simulations, although the relative effect is respected in terms of the increase in heat flux due to blowing. Most of the error can therefore be attributed to the Fay-Riddell model used to calculate the reference heat flux without blowing $\phi_{NB,stag}$. To examine the accuracy of the reduced model developed in this work, the evolution of the model output $(\phi/\phi_{NB})_{stag}$ (red curve) is compared with the CFD simulations (black squares) in Figure 10b. Overall, CFD and ARES simulations are in good agreement. However, the model shows strong variations with altitude, especially around 40 – 50 km, which do not match the trend of CFD simulations.

As a reminder, the Sphere #4 has a nose radius $R_N = 0.6$ m, and the learning database was developed on a design space $R_N \in [0.1, 5.5]$ m, see Table 1. As a test, we trained another model by MFK on a design space reduced to $R_N \in [0.1, 2.0]$ m, representing 73 CFD-HF points and 280 CFD-LF points. ARES simulations are carried out with this new model. The evolution of $\phi_{NB,stag}$ shows little deviation from the initial model, see Figure 11a. In contrast, the evolution of $(\phi/\phi_{NB})_{stag}$ is smoother, and better follows the global trend of CFD simulations. This is also true for the other COPV geometries studied but not shown.

A first hypothesis is that the difference between the initial and the test models may be due to an overfitting of the initial model, which was trained on 708 CFD-LF points and 180 CFD-HF points. This seems unlikely, as pro-

Table 2: Dimensions of considered COPV.

Name	D [mm]	L [mm]	r [mm]	m_{ini} [kg]	α [°]
Sphere #1	200	-	-	2.1	-
Sphere #2	500	-	-	14.3	-
Sphere #3	1000	-	-	58.5	-
Sphere #4	1200	-	-	84.7	-
Spherical-cylinder #1	400	100	-	11.4	0
Spherical-cylinder #2	1500	650	-	191.2	0
Spherical-cylinder #3	1200	1650	-	203.0	0
Spherical-cylinder #4	400	100	-	11.4	90
Spherical-cylinder #5	1500	650	-	191.2	90
Spherical-cylinder #6	1200	1650	-	203.0	90
Tank JAXA	1000	1261	264	35.2	45

Table 3: Flight conditions for CFD simulations.

z [km]	V_∞ [$\text{m} \cdot \text{s}^{-1}$]	p_∞ [Pa]	T_∞ [K]	T_w [K]	\dot{m} [$\text{kg} \cdot \text{m}^{-2} \cdot \text{s}^{-1}$]
72.5	6660.33	3.55	213.29	1498.66	12.18×10^{-3}
70.0	6359.65	5.22	219.58	1566.63	13.46×10^{-3}
67.5	6048.13	7.60	226.44	1646.87	14.07×10^{-3}
65.0	5714.08	10.93	233.29	1701.73	14.65×10^{-3}
62.5	5351.97	15.57	240.15	1734.35	15.04×10^{-3}
60.0	4960.32	21.96	247.02	1722.02	15.21×10^{-3}
57.5	4541.06	30.70	253.89	1646.90	15.16×10^{-3}
55.0	4099.14	42.53	260.77	1629.76	14.88×10^{-3}
52.5	3642.57	58.44	267.65	1601.50	14.42×10^{-3}
50.0	3182.33	79.78	270.65	1445.44	13.87×10^{-3}
47.5	2723.14	108.87	270.65	1345.02	13.25×10^{-3}
45.0	2273.58	149.12	264.16	1198.11	12.52×10^{-3}
42.5	1840.07	205.99	257.26	1046.85	11.68×10^{-3}

gressively reducing the size of the training base while maintaining the bounds of the design space, still results in strong oscillations for $(\phi/\phi_{NB})_{stag}$ at low altitude, as in Figure 10b.

A second hypothesis is that there are different physical regimes over the entire design space, which cannot be modeled in a unified way by a single model. In particular, chemical relaxation phenomena are very different depending on flight conditions. For an object with a small nose radius, at high altitude and high speed, the flow will be in chemical non-equilibrium, or even chemically frozen. On the contrary, for an object with a large nose radius, at low altitude and speed, the flow is in chemical equilibrium, with a behavior close to that of a perfect gas. It is quite possible that the phenomena underlying the effects of pyrolysis gas blowing on heat flux modification are too strongly linked to chemical relaxation effects to allow the development of a single reduced order model using MFK, valid over the entire design space defined in Table 1. By limiting $R_N \in [0.1, 2.0]$ m during the test model training, a large number of cases at chemical equilibrium have been eliminated, perhaps explaining why this model gives a satisfactory prediction. Further investigations are required here.

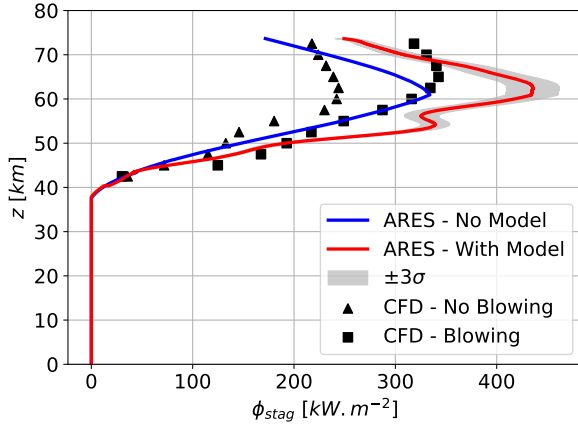
4. CONCLUSIONS AND PERSPECTIVES

A surrogate model has been developed using Multi-Fidelity Kriging to predict the influence of pyrolysis gas blowing on the modification of stagnation point wall heat flux. This choice has been made after defining the inputs/output of the desired model and the size of the training database. The training database is made of two nested Latin hypercubes, with low-fidelity CFD simulations (CFD-LF), and high-fidelity CFD simulations (CFD-HF). The surrogate model is trained, and its RMSE is evaluated to 19.21% on the validation dataset. However, the prediction error is only 10.84% when evaluated on the part of the validation dataset verifying $\phi_{NB,stag} \geq 50 \text{ kW} \cdot \text{m}^{-2}$. The model is implemented in the atmospheric re-entry code ARES. Re-entry trajectories from LEO of different COPV geometries have been computed, and reveal a significant increase of about 30% in the integrated stagnation point wall heat flux during the continuous regime. This assesses the major influence of pyrolysis gas blowing during re-entry of carbon-polymer composite materials.

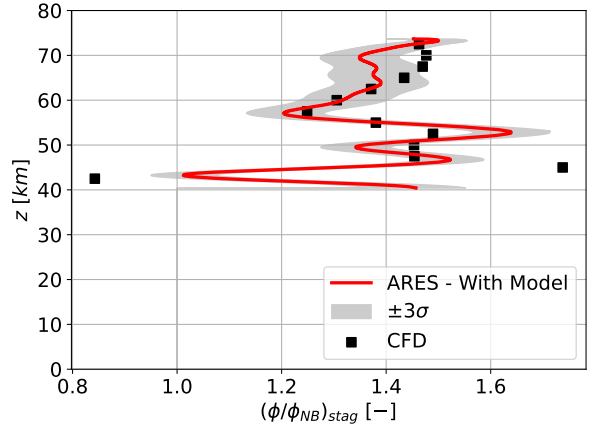
However, the model predicts strong oscillations for $(\phi/\phi_{NB})_{stag}$ at low altitudes $z \leq 50$ km. Our hypothesis is that chemical relaxation phenomena undergoes different regimes over the entire design space, which cannot be

Table 4: Integrated stagnation point wall heat flux during the continuous regime for considered COPV, with or without activation of the surrogate model to take into account the influence of pyrolysis gas blowing on heat transfer modification. Relative difference is reported in the last column. Data with activation of the surrogate model are given with the 99 % confidence interval ($\pm 3\sigma$).

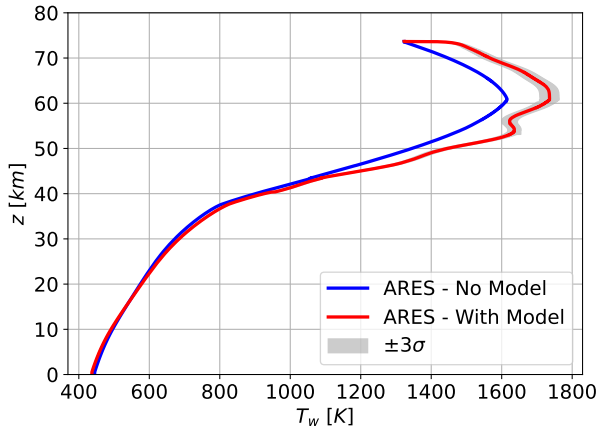
COPV geometries	Without model	With model	
	$[\text{J} \cdot \text{m}^{-2}]$	$[\text{J} \cdot \text{m}^{-2}]$	[%]
Sphere #1	1.63×10^7	$(2.03 \pm 0.14) \times 10^7$	24.6 ± 8.7
Sphere #2	2.45×10^7	$(3.37 \pm 0.21) \times 10^7$	37.5 ± 8.4
Sphere #3	2.64×10^7	$(3.63 \pm 0.16) \times 10^7$	37.2 ± 6.2
Sphere #4	2.66×10^7	$(3.56 \pm 0.18) \times 10^7$	33.7 ± 6.7
Spherical-cylinder #1	3.48×10^7	$(4.80 \pm 0.30) \times 10^7$	37.7 ± 8.7
Spherical-cylinder #2	4.45×10^7	$(5.90 \pm 0.23) \times 10^7$	32.3 ± 5.1
Spherical-cylinder #3	7.63×10^7	$(1.01 \pm 0.05) \times 10^8$	32.8 ± 6.3
Spherical-cylinder #4	1.63×10^7	$(2.21 \pm 0.10) \times 10^7$	35.0 ± 6.0
Spherical-cylinder #5	1.92×10^7	$(2.57 \pm 0.12) \times 10^7$	33.6 ± 6.0
Spherical-cylinder #6	1.68×10^7	$(2.22 \pm 0.10) \times 10^7$	32.5 ± 5.8
Tank JAXA	5.13×10^7	$(6.94 \pm 0.37) \times 10^7$	35.2 ± 7.1



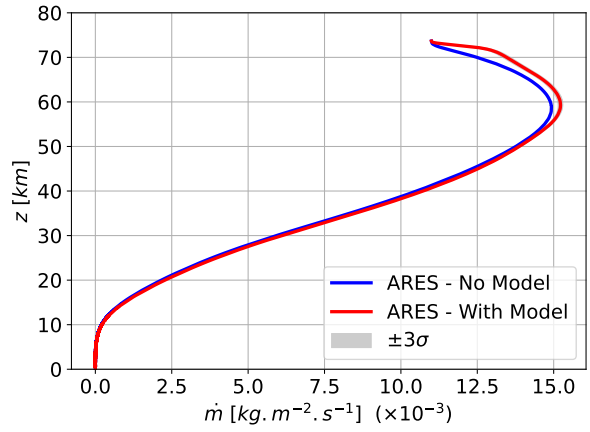
(a) Convective-diffusive heat flux ϕ_{stag} .



(b) Surrogate model output $(\phi/\phi_{NB})_{stag}$.

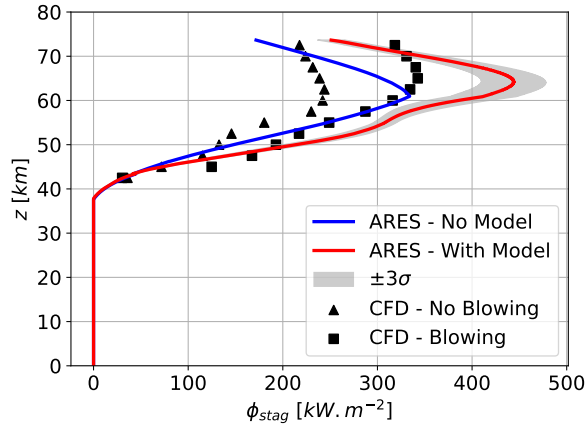


(c) Wall temperature T_w .

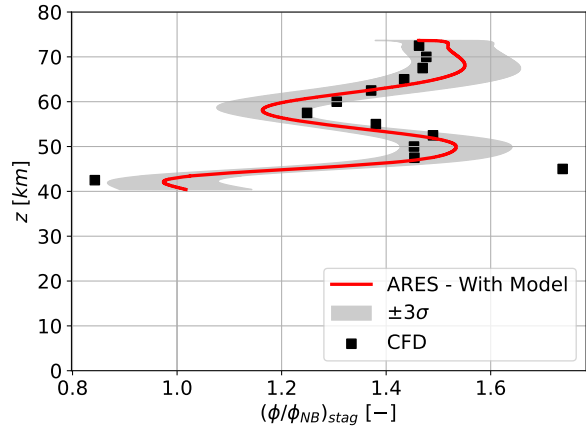


(d) Pyrolysis gas mass blowing rate \dot{m} .

Figure 10: Evolution of several quantities at stagnation point with respect to altitude z in the continuous regime for sphere #4 of Table 2. Solid colored lines correspond to atmospheric re-entry simulations, with (red) or without (blue) activation of the surrogate model developed in this work. Black symbols correspond to CFD simulations with (square) or without (triangle) blowing.



(a) Convective-diffusive heat flux ϕ_{stag} .



(b) Surrogate model output $(\phi/\phi_{NB})_{stag}$.

Figure 11: Evolution of several quantities at stagnation point with respect to altitude z in the continuous regime for sphere #4 of Table 2. Solid colored lines correspond to atmospheric re-entry simulations, with (red) or without (blue) activation of the surrogate model trained on 73 CFD-HF points and 280 CFD-LF points, such as $R_N \in [0.1, 2.0]$ m. Black symbols correspond to CFD simulations with (square) or without (triangle) blowing.

modeled in a unified way by a single model. Further investigations are needed to characterise the chemical equilibrium state in the shock layer. If several regimes are indeed identified, one perspective is to perform data clustering during the training process. In addition, the adaptive addition of training points in areas of the design space with large prediction error should improve model accuracy. Finally, this model is developed assuming constant pyrolysis gas composition. New models could be trained for different compositions following our methodology. A more interesting approach would be to train a more complete model, taking the blowing chemical composition as inputs.

ACKNOWLEDGMENTS

This work was supported by the ONERA and "Centre National d'Études Spatiales" (French Space Agency) through the co-funding of the PhD of M. Lalande.

REFERENCES

1. European Space Agency. ESA's Re-Entry Predictions, Recovered Debris. URL <https://reentry.esoc.esa.int/home/recovereddebris>. Consulted on 05/04/2023.
2. H. Alkandry, I.D. Boyd, and A. Martin. Comparison of Transport Properties Models for Flowfield Simulations of Ablative Heat Shields. *Journal of Thermophysics and Heat Transfer*, 28(4):569–582, 2014. doi: 10.2514/1.T4233.
3. G.V. Candler, C.R. Alba, and R.B. Greendyke. Characterization of Carbon Ablation Models Including Effects of Gas-Phase Chemical Kinetics. *Journal of Thermophysics and Heat Transfer*, 31(3):512–526, 2017. doi: 10.2514/1.T4752.
4. S.-S. Chen, F.-J. Cai, H.-C. Xue, N. Wang, and C. Yan. An Improved AUSM-Family Scheme with Robustness and Accuracy for all Mach Number Flows. *Applied Mathematical Modelling*, 77:1065–1081, 2020. doi: 10.1016/j.apm.2019.09.005.
5. N. Dellinger, G. Leplat, C. Huchette, V. Biasi, and F. Feyel. Numerical Modeling and Experimental Validation of Heat and Mass Transfer Within decomposing Carbon Fibers/Epoxy Resin Composite Laminates. *International Journal of Thermal Sciences*, 2024.
6. R.W. Detra and H. Hidalgo. Generalized Heat Transfer Formulas and Graphs for Nose Cone Re-Entry Into the Atmosphere. *ARS Journal*, 31(3):318–321, 1961. doi: 10.2514/8.5471.
7. R.W. Detra, N.H. Kemp, and F.R. Riddell. Addendum to Heat Transfer to Satellite Vehicle Reentering the Atmosphere. *Jet Propulsion*, 27(12):1256–1257, 1957.
8. A. Ern and V. Giovangigli. *Multicomponent Transport Algorithms*, volume 24. Springer Science & Business Media, 1994.
9. A. Ern and V. Giovangigli. Fast and Accurate Multicomponent Transport Property Evaluation. *Journal of Computational Physics*, 120(1):105–116, 1995. doi: 10.1006/jcph.1995.1151.
10. J.A. Fay and F.R. Riddell. Theory of Stagnation Point Heat Transfer in Dissociated Air. *Journal of the Aerospace Sciences*, 25(2):73–85, 1958. doi: 10.2514/8.7517.
11. L. Gkimitis, B. Dias, J.B. Scoggins, T. Magin, M. A Mendez, and A. Turchi. Data-Driven Modeling of

- Hypersonic Reentry Flow with Heat and Mass Transfer. *AIAA Journal*, 61(8):3269–3286, 2023. doi: 10.2514/1.J062332.
12. P. Gnoffo. Multi-Dimensional Inviscid Flux Reconstruction for Simulation of Hypersonic Heating on Tetrahedral Grids. In *47th AIAA Aerospace Sciences Meeting including The New Horizons Forum and Aerospace Exposition*, page 599, 2009. doi: 10.2514/6.2009-599.
 13. N.H. Kemp and F.R. Riddell. Heat Transfer to Satellite Vehicles Re-Entering the Atmosphere. *Journal of Jet Propulsion*, 27(2):132–137, 1957. doi: 10.2514/8.12603.
 14. K.H. Kim, J.H. Lee, and O.H. Rho. An Improvement of AUSM Schemes by Introducing the Pressure-Based Weight Functions. *Computers & fluids*, 27(3):311–346, 1998. doi: 10.1016/S0045-7930(97)00069-8.
 15. K. Kitamura and E. Shima. Towards Shock-Stable and Accurate Hypersonic Heating Computations: A New Pressure Flux for AUSM-Family Schemes. *Journal of Computational Physics*, 245:62–83, 2013. doi: 10.1016/j.jcp.2013.02.046.
 16. D.W. Kuntz, B. Hassan, and D.L. Potter. Predictions of Ablating Hypersonic Vehicles Using an Iterative Coupled Fluid/Thermal Approach. *Journal of Thermophysics and Heat Transfer*, 15(2):129–139, 2001. doi: 10.2514/2.6594.
 17. M. Lalande, N. Dellinger, Y. Prévereaud, and N. Bartoli. Assessment of Thermochemical Degradation Effects of Charring Material on the Wall Heat Flux during Atmospheric Re-Entry. In *HiSST: 3rd International Conference on High-Speed Vehicle Science & Technology*, page 140, 2024.
 18. M. Lalande, N. Dellinger, Y. Prévereaud, and N. Bartoli. Assessment of Air-Pyrolysis Gas Reactions on the Wall Heat Flux during Atmospheric Re-Entry. *International Journal of Heat and Mass Transfer*, (submitted), 2025.
 19. M. Lalande, N. Dellinger, Y. Prévereaud, N. Bartoli, and J.-M. Lamet. Blottner’s Coefficients and Prandtl Number for Charring Materials Atmospheric Entry Simulations. *AIAA Journal*, Technical Note, in review., 2025.
 20. L. Le Gratiet. *Multi-Fidelity Gaussian Process Regression for Computer Experiments*. PhD thesis, Université Paris-Diderot (Paris VII), France, 2013.
 21. C. Le Touze, A. Murrone, and H. Guillard. Multislope MUSCL Method for General Unstructured Meshes. *Journal of Computational Physics*, 284:389–418, 2015. doi: 10.1016/j.jcp.2014.12.032.
 22. N. Leterrier. *Discrétisation spatiale en maillage non-structuré de type général*. PhD thesis, Paris 6, 2003.
 23. M.-S. Liou. A Sequel to AUSM: AUSM+. *Journal of Computational Physics*, 129(2):364–382, 1996. doi: 10.1006/jcph.1996.0256.
 24. T. Lips, B. Fritsche, R. Kanzler, T. Schleutker, A. Gülhan, B. Bonvoisin, T. Soares, and G. Sinema. About the Demisability of Propellant Tanks During Atmospheric Re-Entry From LEO. *Journal of Space Safety Engineering*, 4(2):99–104, 2017. doi: 10.1016/j.jsse.2017.07.004.
 25. A. Martin and I.D. Boyd. Modeling of Heat Transfer Attenuation by Ablative Gases During the Stardust Reentry. *Journal of Thermophysics and Heat Transfer*, 29(3):450–466, 2015. doi: 10.2514/1.T4202.
 26. A. Martin, I. Cozmuta, M.J. Wright, and I.D. Boyd. Kinetic Rates for Gas-Phase Chemistry of Phenolic-Based Carbon Ablator in Atmospheric Air. *Journal of Thermophysics and Heat Transfer*, 29(2):222–240, 2015. doi: 10.2514/1.T4184.
 27. N. Perron. *Modélisation de la Dégradation Thermo-Structurale des Débris Spatiaux durant la Rentrée Atmosphérique*. PhD thesis, Université de Toulouse (ISAE), France, 2022.
 28. Y. Prévereaud. *Contribution à la Modélisation de la Rentrée Atmosphérique des Débris Spatiaux*. PhD thesis, Université de Toulouse (ISAE), France, 2014.
 29. Y. Prévereaud, J.L. Vérant, and J. Annaloro. Noncatalytic and Finite Catalytic Heating Models for Atmospheric Re-entry Codes. In *First International Orbital Debris Conference (IOC)*, 2019. URL <https://hal.science/hal-02443767>.
 30. C.E. Rasmussen and C. Williams. *Gaussian Processes for Machine Learning*. Cambridge, MA: MIT Press, 2006.
 31. Jens A Rataczak, Iain D Boyd, and Jay W McMahon. Surrogate Models for Hypersonic Aerothermodynamics and Aerodynamics using Gaussian Process Regression. In *AIAA SCITECH 2024 Forum*, page 0461, 2024. doi: 10.2514/6.2024-0461.
 32. A. Refloch, B. Courbet, A. Murrone, P. Villedieu, C. Laurent, P. Gilbank, J. Troyes, L. Tessé, G. Chainerau, J.B. Dargaud, et al. CEDRE Software. *Aerospace Lab*, (2), 2011.
 33. P. Sagnier and J.L. Vérant. Flow Characterization in the ONERA F4 High-Enthalpy Wind Tunnel. *AIAA Journal*, 36(4):522–531, 1998. doi: 10.2514/2.425.
 34. P. Saves, R. Lafage, N. Bartoli, Y. Diouane, J. Bussemaker, T. Lefebvre, J.T. Hwang, J. Morlier, and J. R. A. Martins. SMT 2.0: A Surrogate Modeling Toolbox with a focus on Hierarchical and Mixed Variables Gaussian Processes. *Advances in Engineering Software*, 188:103571, 2024. doi: 10.1016/j.advengsoft.2023.103571.
 35. M. Schouler, Y. Prévereaud, and L. Mieussens. Machine Learning Based Reduced Models for the Aerothermodynamic and Aerodynamic Wall Quantities in Hypersonic Rarefied Conditions. *Acta Astronautica*, 204:83–106, 2023. doi: 10.1016/j.actaastro.2022.12.039.
 36. C.D. Scott, R.C. Ried, R.J. Maraia, C.P. Li, and S.M. Derry. An AOTV Aeroheating and Thermal Protection Study. In *19th Thermophysics Conference*, page 1710, 1984. doi: 10.2514/6.1984-1710.

37. K. Sutton and R.A. Jr Graves. A General Stagnation-Point Convective Heating Equation for Arbitrary Gas Mixtures. Technical Report NASA-TR-R-376, NASA Langley Research Center, 1971.
38. F. Torres-Herrador, A. Eschenbacher, J. Blondeau, T.E. Magin, and K.M. Van Geem. Study of the Degradation of Epoxy Resins Used in Spacecraft Components by Thermogravimetry and Fast Pyrolysis. *Journal of Analytical and Applied Pyrolysis*, 161: 105397, 2022. doi: 10.1016/j.jaap.2021.105397.
39. C.R. Wilke. A Viscosity Equation for Gas Mixtures. *The Journal of Chemical Physics*, 18(4):517–519, 1950. doi: 10.1063/1.1747673.